Earth Planet. Sci. Lett. 638 (2024) 118762

Contents lists available at ScienceDirect

Earth and Planetary Science Letters

journal homepage: www.elsevier.com/locate/epsl

The early onset of magmatic rift faulting in the Edward-George Rift, Uganda

Luke N.J. Wedmore [a,§], Dan Evans [a,§], Jack N. Williams [b,*], Juliet Biggs [a], Åke Fagereng [c], Peter Mawejje [d], Fred Tugume [d], Thomas Blenkinsop [c], Daniel E.J. Hobley [c,e]

[a] Department of Earth Sciences, University of Bristol, Bristol United Kingdom
[b] Department of Geology, University of Otago, Dunedin, New Zealand
[c] School of Earth and Environmental Sciences, Cardiff University, Cardiff, United Kingdom
[d] Directorate of Geological Survey and Mines, Uganda
[e] RSK ADAS Ltd, Helsby, Cheshire, United Kingdom

ARTICLE INFO

Keywords:
Continental rifting
East African Rift
Albertine Rift
Fault growth
Magmato-tectonic interactions

ABSTRACT

Fault systems along slow-spreading mid-ocean ridges have a characteristic morphology including clustered, closely spaced, short faults, which emerges during the preceding phase of magma-assisted continental rifting and breakup. Current observations of faulting in magmatic rifts are, however, limited to mature magma-rich rifts where the early phases of rifting are obscured by later sedimentary and volcanic deposits. Thus, it is unclear how and when fault networks first evolve in magmatic rifts. Here, we investigate the Edward-George Rift, Uganda, where crustal thinning is minimal and surface volcanism is less than 200 ka. Using high resolution topography, we map and compile a database of 152 active faults, and systematically measure scarp heights along each fault. A region of high density (up to 2 km/km^2) short (79% <5 km) intrabasin faults, with strikes rotated ~45° from the regional tectonic stress field, is co-located with a mid-crustal magma body. Scarp height-length profiles demonstrate that 81% of faults experience laterally-restricted propagation and appear to propagate away from magmatic bodies. Magmatism influences fault growth by reducing the differential and effective stresses, and/or changing the material properties of the crust surrounding the faults. Comparisons with other fault systems suggests that fault density increases as rifting evolves, but that high-density fault networks dominated by short faults are formed rapidly at the onset of magmatic rifting and persist until sea-floor spreading.

1. Introduction

Magmatic rifting is instrumental in facilitating continental breakup, as it allows rifting to proceed even though tectonic forces are not sufficient to overcome the strength of intact lithosphere (Buck, 2004; Kendall et al., 2005). Unique patterns of faulting and deformation are established in magmatic rifts, which ultimately control the morphology of fault systems along ensuing mid-ocean ridges (Wolfenden et al., 2005; Illsley-Kemp et al., 2017). Rifting often initiates in amagmatic regions, and only transitions to magmatic rifting when the upwelling asthenosphere undergoes decompression melting. This melt production induces thermal and mechanical changes to the crust that produce rift segments notable for a high density of short faults compared with amagmatic rift segments, which are typically dominated by long, large offset border faults. However, establishing how and when this transition from amagmatic to magmatic rifting occurs, and the exact mechanism that induces the dramatic change in rift morphology has proved challenging, because the earliest phases of magmatic rifting are often obscured by subsequent volcanic or sedimentary deposits.

Prior to magmatism, and also in rifts that remain magma-poor throughout their lifetime, faults grow through a combination of crack propagation and segment linkage (Rotevatn et al., 2019). In turn, there are several characteristics of rift faults that reflect this growth process: i) the establishment of a fault's full length at an early stage of displacement accumulation (e.g., Rotevatn et al., 2019), ii) fault systems start as distributed networks of diffuse faulting before evolving to a network with a low density of active faults and a higher number of long faults (Cowie, 1998); iii) border faults at the edge of rifts that are

* Corresponding author.
§ Joint first authors.
E-mail address: jack.williams@otago.ac.nz (J.N. Williams).

https://doi.org/10.1016/j.epsl.2024.118762
Received 5 July 2023; Received in revised form 4 April 2024; Accepted 7 May 2024
Available online 17 May 2024
0012-821X/© 2024 The Author(s). Published by Elsevier B.V. This is an open access article under the CC BY license (http://creativecommons.org/licenses/by/4.0/).

geometrically segmented and accommodate a large amount of cumulative displacement (Ebinger, 1989; Muirhead et al., 2019); and iv) fault displacement profiles that depart from the elliptical shapes excepted for a fault growing through crack propagation alone, and instead have displacement minima at segment boundaries (Cartwright et al., 1995). In detail, however, these characteristics can be influenced by factors such as pre-existing crustal fabrics (Samsu et al., 2023) and the mechanical thickness and lithology that the faults are forming in (Ackermann et al., 2001; Buck, 2004).

Fault systems at mature magmatic continental rifts and mid-ocean ridges, especially at slow spreading ridges, are distinct from those at amagmatic rifts. They typically have: i) clusters of closely spaced subparallel faults with increasing fault density surrounding magmatic centres (Shaw, 1992; Dumont et al., 2019); ii) fault systems dominated by short faults with exponential fault-length frequency distributions (Cowie et al., 1993; Gupta and Scholz, 2000); iii) localised surface deformation at the rift axis (Ebinger and Casey, 2001; Escartín et al., 2014); iv) a range of fault displacement profile shapes, albeit asymmetric triangular profiles are generally dominant (Manighetti et al., 2001; Dumont et al., 2017); and v) extension accommodated by a combination of dyke intrusions, normal faults and fissures (Rowland et al., 2007; Bubeck et al., 2018). At the onset of magmatic rifting, the rise of buoyant magma heats the lithosphere, which reduces the depth to the frictional-viscous transition (White and McKenzie, 1989; Daniels et al., 2014). At the same time, magmatic intrusions into the crust reduce its strength (i.e., the differential stress that is required to be exceeded for failure; Buck, 2004), and the exsolution of volatiles at mantle depths, and the circulation of these volatiles and other hydrothermal fluids through the crust (Lee et al., 2016), mechanically weakens the crust by reducing the effective stress (i.e. the lithostatic stress minus the pore

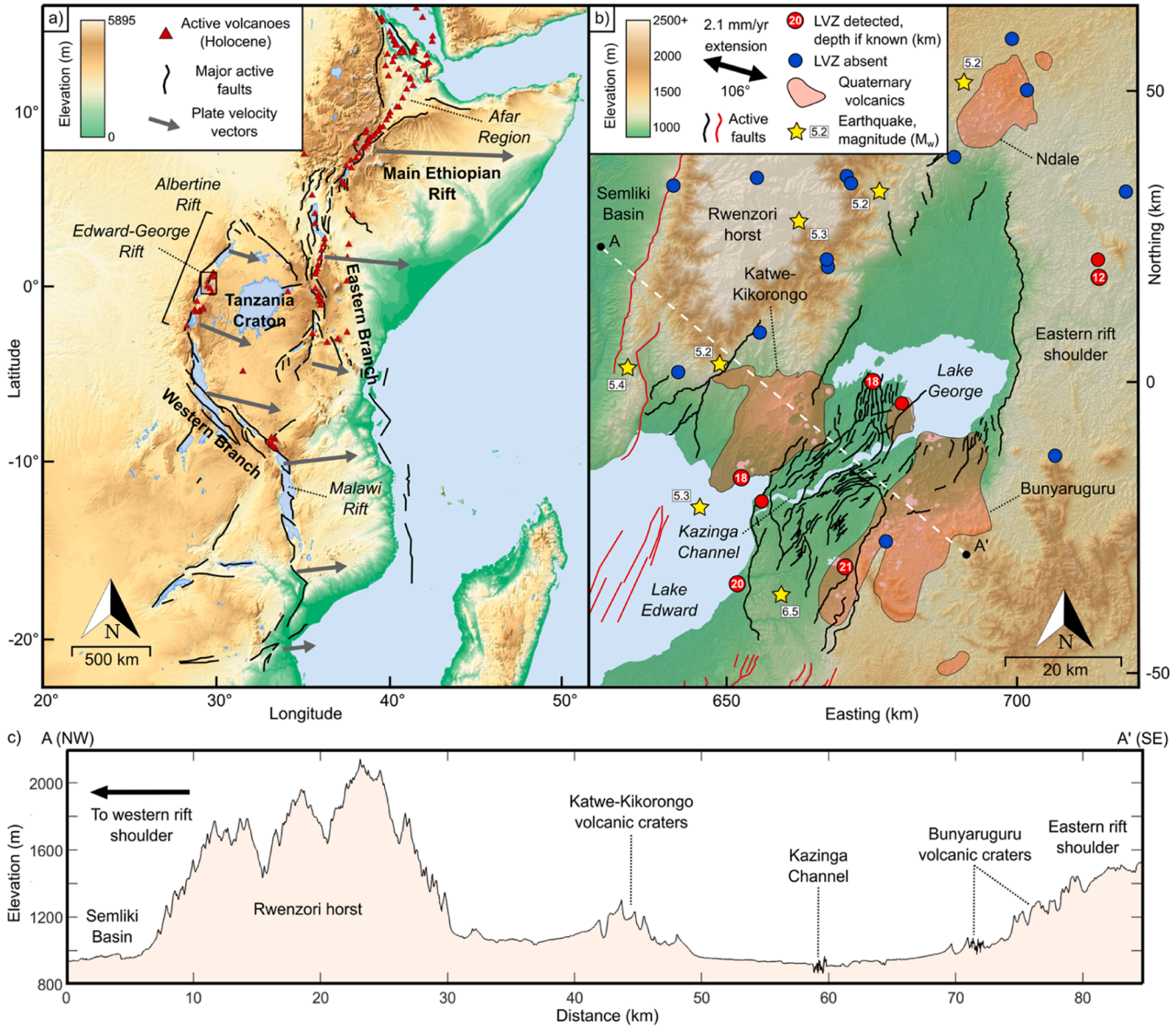

Fig. 1. (a) Topographic map of the East African Rift System. Black lines mark major active faults, red triangles mark Holocene active volcanoes; grey arrows show scaled plate velocity vectors (Stamps et al. 2008). (b) The Edward-George Rift with black lines showing faults mapped and analysed in this study, and red lines for other faults in the Semliki and central Lake Edward basins that fall outside of the study area. Faults mapped under Lake Edward after McGlue et al. (2006). The extent of a mid-crustal LVZ is outlined by seismic stations, shown as red (LVZ detected) and blue (LVZ absent) markers (Wölbern et al., 2010; Gummert et al., 2016). The extent of Quaternary Toro-Ankole volcanics is modified from Rosenthal et al., 2009). Hypocentres of historical >M_w 5 earthquakes are marked as yellow stars and labelled with magnitude. (c) NW-SE topographic cross-section highlighting key morphological features of the study area, indicating ~200 m uplift on the eastern flank of the Edward-George Rift.

fluid pressure). Mechanical and thermal changes to crustal strength such as these affect the growth of faults and the distribution of deformation. For example, in volcanic rift systems, the distribution and geometry of active faults are thought to be linked to the supply of magma at depth (Muirhead et al., 2016; Bubeck et al., 2018; Koehn et al., 2019), and fluid flow in faults systems is known to lead to failure of smaller faults, which in turn increases seismic b-values (King, 1983; Cox, 2016). Thus, magmatism fundamentally changes how rifts deform. However, it remains unclear how and when these changes first occur as few studies have documented the fault networks of magmatic rifts where crustal thinning is minimal and magmatism has only recently commenced.

Here we investigate a fault network that has formed contemporaneously with surface volcanism in Uganda between lakes Edward and George, an area we refer to as the Edward-George Rift (Fig. 1a). This rift is located near the northern end of the Western Branch of the East African Rift System (EARS), at the nexus between the amagmatic rifts of the southern EARS (e.g. Ebinger, 1989; Muirhead et al., 2019; Williams et al., 2022) and magma-rich rift segments along the Eastern Branch of the EARS (Ebinger, 2005; Muirhead et al., 2015). The oldest known volcanic rocks in the Edward-George Rift are ~190 ka (Boven et al., 1998; Pitcavage et al., 2021) and there has been minimal crustal thinning (Wölbern et al., 2010). Thus, it is the ideal location to analyse a fault network during early magmatic rifting. We mapped 152 active faults and measured the height of their scarps to analyse the role of magmatism and regional tectonics on the development of the Edward-George Rift. We then compare the properties of this fault network with other well-mapped fault networks along the East African Rift.

2. Geological setting

2.1. The East African Rift System

The ~3000 km-long East African Rift System (EARS) comprises a series of linked rift segments that accommodate extension between the Nubian, Somalian, Victorian, Rovuma, and San plates (Stamps et al., 2021; Wedmore et al., 2021; Fig. 1a). The EARS is split into the Western and Southwestern branches and the Main Ethiopian Rift (MER) and Eastern Branch (Figure 1a; Ebinger, 2005). In low cumulative strain segments of the Western and Southwestern branches, such as the Malawi and Okavango rifts, there is little to no magmatism, limited crustal thinning (<2–5 km), and fault systems contain long (>80 km) large-offset border faults that accommodate a high (>50%) proportion of strain at the rift edge (Kinabo et al., 2008; Njinju et al., 2019; Wedmore et al., 2020; Sun et al., 2021; Williams et al., 2022). In the MER, where cumulative strain is highest along the EARS, strain is generally concentrated at the rift axis (Ebinger and Casey, 2001) and active fault systems are dominated by short fault segments (Agostini et al., 2011). Volcanism along the MER is widespread (Biggs et al., 2021), although direct evidence of dike intrusions is rare (Temtime et al., 2020). Many of these fault characteristics are also observed in mature magmatic rift segments along proto sea-floor spreading segments in the Afar Rift (Manighetti et al., 2001; Dumont et al., 2017, 2019) and mid-ocean ridge fault systems (Escartín et al., 2014).

Axial rifting along smaller intrarift faults has also been documented in magmatic sections of the EARS Eastern Branch (Ebinger, 2005; Muirhead et al., 2016). However, even in relatively young Eastern Branch segments, such as the Magadi and Natron basins, there has been 5–10 km crustal thinning (Plasman et al., 2017), km-thick synrift sediments have accumulated, and surface volcanism is >1 Ma (Muirhead et al., 2016). This implies that the earliest phases of magmatic rifting in these segments may have been obscured by subsequent volcanic and synrift deposits, and hence the processes that control changes in the distribution of strain, fault length, fault orientation and fault density compared with magma-poor rifts remain unclear.

2.2. The Edward-George Rift

In contrast to extensive magmatism along much of the MER and Eastern Branch, the EARS Western Branch contains just four volcanic provinces (Ebinger, 1989). We focus here on the Toro-Ankole volcanic province, which is located in the Albertine Rift near the northern end of the Western Branch (Fig. 1a). The Albertine Rift trends NNE-SSW and is undergoing 2.1 mm/yr of WNW-ESE extension (~106°; Stamps et al., 2008). Major rifting in the Albertine Rift had commenced by the Miocene (Simon et al., 2017) and possibly as early as the Eocene (Jess et al., 2020). Individual rift segments of the Albertine Rift form grabens and half-grabens, bounded by prominent border faults that have throws of up to ~7 km and are segmented along strike (Upcott et al., 1996; Lærdal and Talbot, 2002). The area between the Lake George and Lake Edward segments is marked by a NE-SW trending accommodation zone (Ebinger, 1989; Lærdal and Talbot, 2002). We refer to this area as the Edward-George Rift and it is the focus of this study.

The crust beneath the Edward-George Rift is ~30 km thick, and is not notably thinned (Wölbern et al., 2010). However, receiver functions and a high b-value indicate that there is an elongated low velocity zone (LVZ) below this rift segment at 12–21 km depth (Figure 1b; Wölbern et al., 2010; Lindenfeld et al., 2012; Gummert et al., 2016; Batte and Rümpker, 2019). The velocity change (v_P/v_S ratio of 1.99 beneath the rift vs ~1.74 on the rift shoulders) is interpreted as a zone of partial melting associated with the Katwe-Kikorongo and Bunyaruguru volcanic fields (Gummert et al., 2016) of the larger Toro-Ankole volcanic province (Fig. 1b-c). Erupted material is volatile-rich and originates from small, closely spaced monogenetic maars (phreatomagmatic craters), thought to be the highest density of explosive craters in the EARS (Delcamp et al., 2019). Compositions are generally indicative of low-degree melting within the lithospheric mantle (Boven et al., 1998; Rosenthal et al., 2009; Pitcavage et al., 2021). The most recent known volcanic activity occurred 4–8 ka and K-Ar/Ar-Ar dating suggests that volcanism must have commenced after 50 ka (Boven et al., 1998). However, there are rare outcrops of extrusive igneous rocks in the Bunyaruguru field that are as old as ~189 ka (Pitcavage et al., 2021).

Faults in the Edward-George Rift form prominent normal fault scarps that offset late Pleistocene-Pliocene rift sediments of alluvial, lacustrine, fluvial and volcanic origin (Lærdal and Talbot, 2002). Seismicity suggests that both intrarift and border faults are currently active (Lindenfeld et al., 2012). Cumulatively, this combination of limited crustal thinning, a mid-crust LVZ, young surface volcanism, and well exposed faults make the Edward-George Rift an ideal location to examine patterns of surface deformation at the transition from amagmatic to magmatic rifting.

3. Data and methods

To determine how surface deformation in the Edward-George Rift has been affected by volcanism and mid-crustal partial melting, we mapped active faults around the region and compiled them in a new database. We also analysed fault displacement profiles, orientations, and fault length-frequency distributions to reveal the mechanics behind the formation and growth of these faults.

3.1. Fault mapping

We used ArcGIS to systematically map onshore faults in and immediately adjacent to the Edward-George Rift by analysing a TanDEM-X digital elevation model (DEM), which has a horizontal resolution of 12.5 m and a vertical error of ±0.2 m (RMSE < 1.4 m; Wessel et al., 2018). This represents an improvement on previous regional fault maps, which relied on Landsat imagery (Lærdal and Talbot, 2002). We define active faults as those that have accommodated displacement within the current EARS tectonic regime as chronostratigraphic data is unavailable for these faults. Examples for EARS offsets include displaced synrift

sedimentary features, such as alluvial fans, terraces, and volcanic edifices, along laterally continuous steep linear scarps (Fig. 2a-b; following Wedmore et al., 2020; Williams et al., 2022). We used geological maps (Baglow et al., 2012b, 2012a), previous literature, and satellite imagery to support our analysis of the high resolution topography (Fig. 2c). Furthermore, we conducted field surveys on selected faults to ground-truth our remote sensing observations and the nature of the offset synrift sediments.

Each fault was mapped as a geographic information system (GIS) line feature, with fault tips defined as the points at which a fault no longer has a detectable topographic expression (Williams et al., 2022). For each fault, we recorded the confidence of activity during the current phase of rifting (binary classification of 1 – low confidence or 2 – high confidence), tip-to-tip fault length, and noted details regarding segmentation, geomorphic expression, and cross-cutting relationships with other faults and sedimentary/volcanic features (Table S1). Splays were mapped as distinct structures, and not included in the fault length analysis. Dip direction was assessed from fault-normal topographic cross sections through the point of steepest gradient. We defined border faults as a fault located at the edge of the rift segment. However, where there were substantial volumes of mapped volcanics (red areas in Fig. 1), we did not identify border faults as these may have been buried. All other faults are intrarift faults.

We calculated fault density as the cumulative length of faults in 2×2 km^2 squares, with a 1 km overlap between squares. To investigate changes in fault orientation along the Edward-George Rift, we measured length-weighted fault azimuths in 10 km wide intervals orientated perpendicular to the GPS-derived regional extension direction (~106°; Stamps et al., 2008) and compare border and intrarift fault azimuth trends.

We then compared the distribution of fault lengths in the Edward-George Rift with other rift settings, as this can reflect whether a fault system is growing by the formation of new faults (power-law distribution) or the coalescence of existing faults (exponential distribution; Gupta and Scholz, 2000). Following the approach of Williams et al. (2022), we first fitted power-law and exponential functions to the empirical fault length data using a Maximum Likelihood Estimator. We then tested the null hypothesis that the empirical fault length cumulative distribution function (cCDF or survival functions) represents a sample from the fitted power law or exponential cCDF using a two-sample Kolmogorov-Smirnov test (with the null hypothesis rejected if $p < 0.1$). As the fault length (l_{min}) below which mapping is incomplete is not known in advance of these tests, we derived the power law and exponential cCDFs for a range of l_{min} values between 0 and 5 km (at 0.2 km increments), and repeated the test for each value of l_{min}. We then compared this Edward-George Rift fault length analysis to an equivalent analysis using fault maps from the Dabahu-Manda-Hararo Rift (Dumont et al., 2017), the Wonji Fault Belt in the Northern Main Ethiopian Rift (Agostini et al., 2011), and Malawi (Williams et al., 2022).

3.2. Along strike scarp height profiles

We measured the height of fault scarps by sampling the DEM in 500 m-long fault-normal profiles at 10 m intervals along strike. These profiles were stacked every 100 m to reduce the effects of short-wavelength topographic features (following Wedmore et al., 2020). We fitted linear regression lines to the hanging wall and footwall slopes for each of the ~4000 stacked profiles and calculated the scarp height as the vertical distance between these two lines at the point of maximum scarp gradient (Figure S1a). We also randomly selected 5% of faults for re-analysis to test the repeatability of our results. As we have no information on the dip angle of the faults or the thickness of hanging wall sediments, we consider the scarp height a minimum estimate of fault displacement. To explore the along-fault variation in scarp height (the displacement profile) we normalised the along-strike scarp height profile for each fault by the maximum scarp height (D_{max}) and length (L_{max}) to enable analysis of its first-order shape irrespective of dimensions. We then visually categorised each fault according to the shapes defined by Manighetti et al. (2001; Fig. 3). For unilaterally-propagating (tip- or half-restricted), double tip-restricted (DTR) and elliptical-with-taper faults that showed a strong sense of preferred propagation, we recorded the dominant propagation direction in our fault attribute table. We assigned each slip profile a clarity grading and noted any segmentation or displacement anomalies.

4. Results

4.1. Fault mapping overview

We mapped 152 fault scarps in the Edward George Rift and immediately adjacent to it in the Lake George and northeast Lake Edward basins (Fig. 1b). The fault traces and their associated attributes have been archived in an open access Zenodo database (https://doi.org/10.5281/zenodo.6510002). Both the border and intrarift faults offset Quaternary-age sediments (Fig. 2, 4, 5& 6). However, although the Nyamwambe Fault, the border fault on the western side of the rift, displaces Quaternary-age alluvial fans (Fig. 4c) and volcanic craters, in some places the fault is fully obscured by volcanic craters (Fig. 4a). In other places, intrarift faults cross-cut and displace volcanic craters (Fig. 4b). Our field observations confirmed the presence of steep active fault scarps with both the border and intrarift faults displacing likely Quaternary-age synrift volcanic, colluvial and lacustrine sediments (Fig. 5).

The faults we have mapped range in length from 0.8 km to 48 km (Fig. 6). The longest faults are border faults including the George Fault (48 km), the Kichwamba Fault (34 km), and the Nyamwambe Fault (20 km). The cumulative frequency distribution of fault lengths reveals a prevalence of relatively short faults (79% <5 km; 52% <2.5 km; Fig. 6d). Fault length is inversely correlated with fault density, such that a high density of short faults (up to ~2 km/km^2) is found around the rift axis, in the region either side of the Kazinga Channel (Fig. 6a). In contrast, the Katwe-Kikorongo and Bunyaruguru volcanic fields towards the rift margins host comparatively lower density faulting (0–1 km/km^2). An additional area with higher density faulting (1–1.5 km/km^2) is located to the southeast of Lake George near the eastern rift shoulder (Fig. 6a). The longest faults (>10 km), which are mostly border faults, are located at the edge of the rift, and generally occur in regions of low fault density. The mean strike of border faults is 016° ± 17° (uncertainty is one standard deviation), and the mean strike of the intrarift faults is 031° ± 23° Thus, for much of the Edward-George Rift, border faults strike approximately perpendicular to the GPS-derived regional tectonic extension direction (~106°; Stamps et al., 2008), whereas the intrarift faults strike sub-perpendicular (Fig. 6). However, intrarift fault azimuths deviate significantly (~45°) from this orientation in the south-central region of the Edward-George Rift, which is the same region as where fault densities are highest and fault lengths shortest (Fig. 6b). Fault azimuths are more scattered (~75° range) at the northern tip of the Lake George basin compared to the rest of the rift (~15–45° range; Fig. 6b).

The cumulative frequency distribution of fault lengths ≥1 km can be fitted by a power law distribution at a statistically significant level (p-value > 0.1; Fig. 6d). Below ~1 km, p-values fall below the 0.1 threshold, suggesting that there is systematic under-sampling of faults <1 km-long (Fig. 6c). No significant fit to an exponential distribution is found, regardless of the minimum fault length used (Fig. 6c).

4.2. Displacement profiles and fault propagation

After removing faults that had large portions of their scarps obscured, 130 out of 152 faults had clear scarp profiles that were suitable for scarp height measurement. The mean residual between the original and the 5% of measurements we repeated is 5 cm, and 83% of

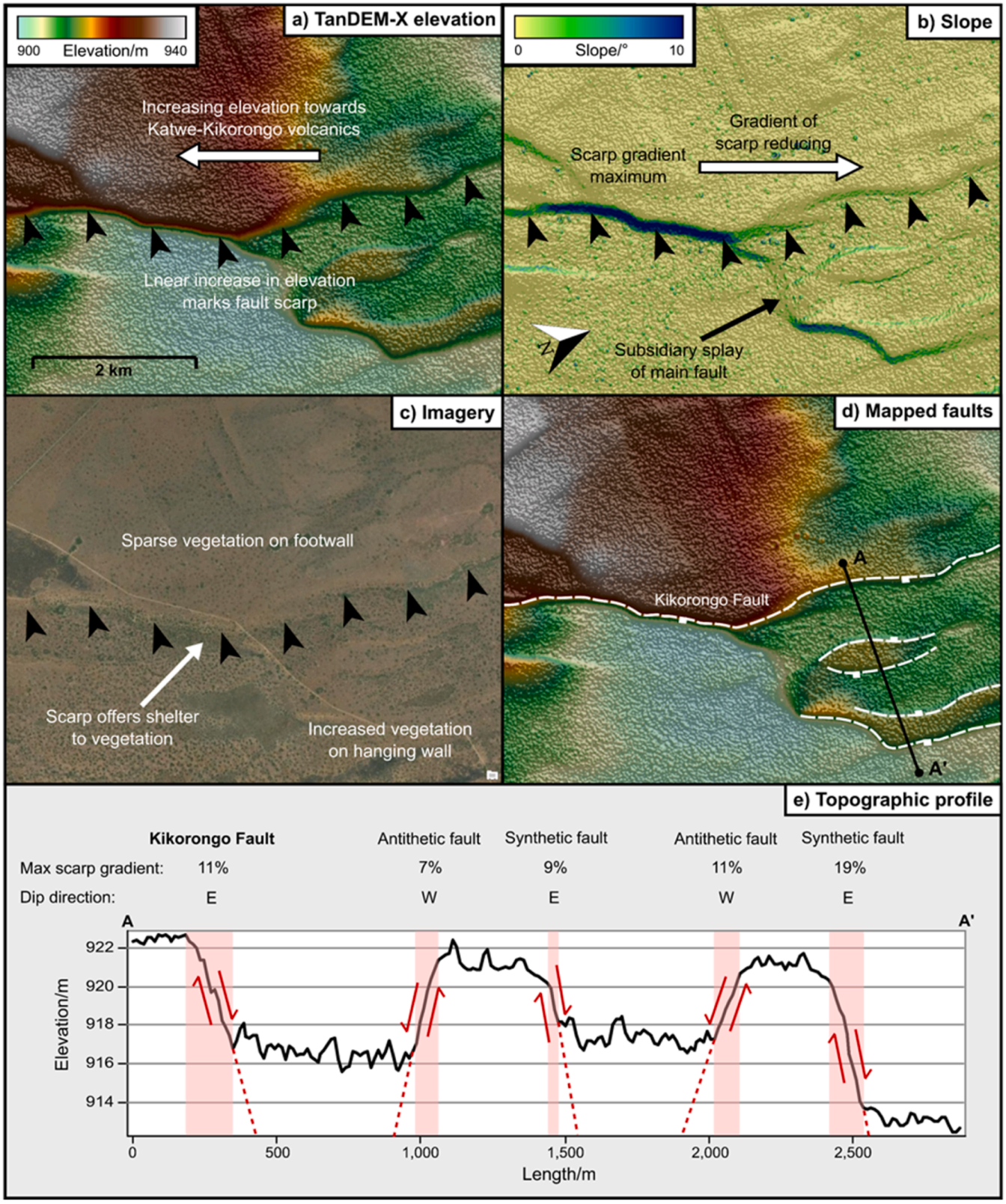

Fig. 2. The method used to identify fault scarps in the Edward-George Rift. Shown here as an example is a section of the Kikorongo Fault. (a) TanDEM-X elevation – the scarp is indicated by a sharp increase in elevation in the footwall. (b) Slope map – a linear increase in slope values corresponds to the scarp. (c) Imagery demonstrates how morphology influences vegetation. (d) Mapped traces of the Kikorongo Fault and subsidiary syn-/antithetic faults. (e) Topographic profiles enable max scarp gradients and dip direction to be calculated. The faults here form a horst and graben structure, with red boxes highlighting each scarp, extrapolated as red dashed lines. Red arrows show the sense of motion on each fault.

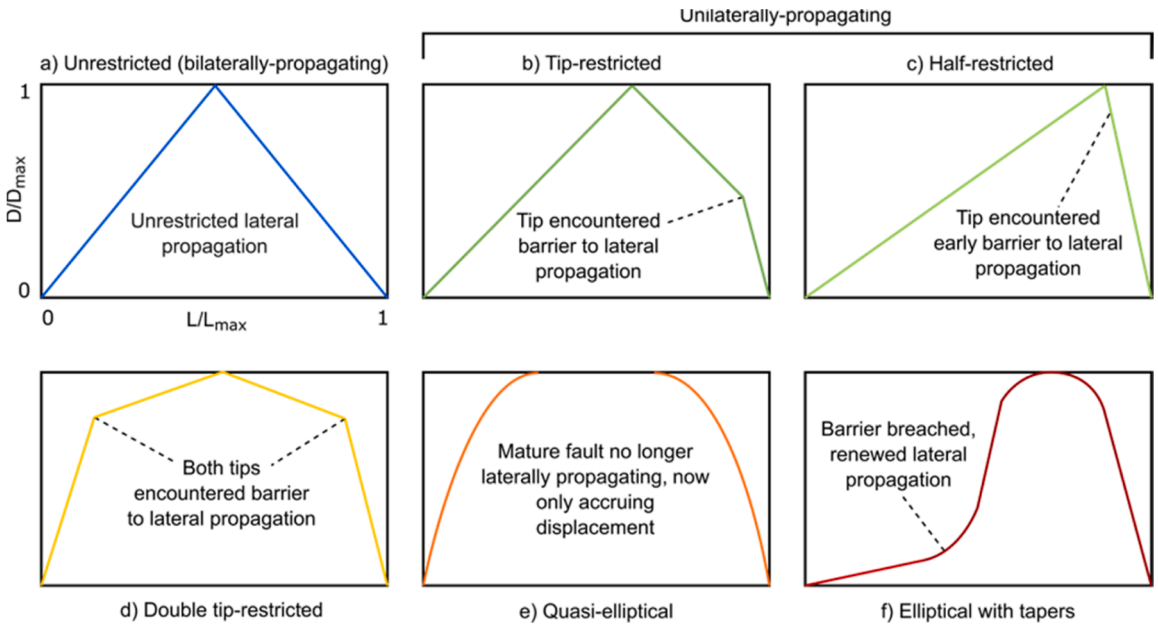

Fig. 3. Fault slip profiles were normalised against their maximum displacement (D_{max}) and length (L_{max}), then categorised into one of six idealised first-order shapes. Adapted from Manighetti et al. (2001).

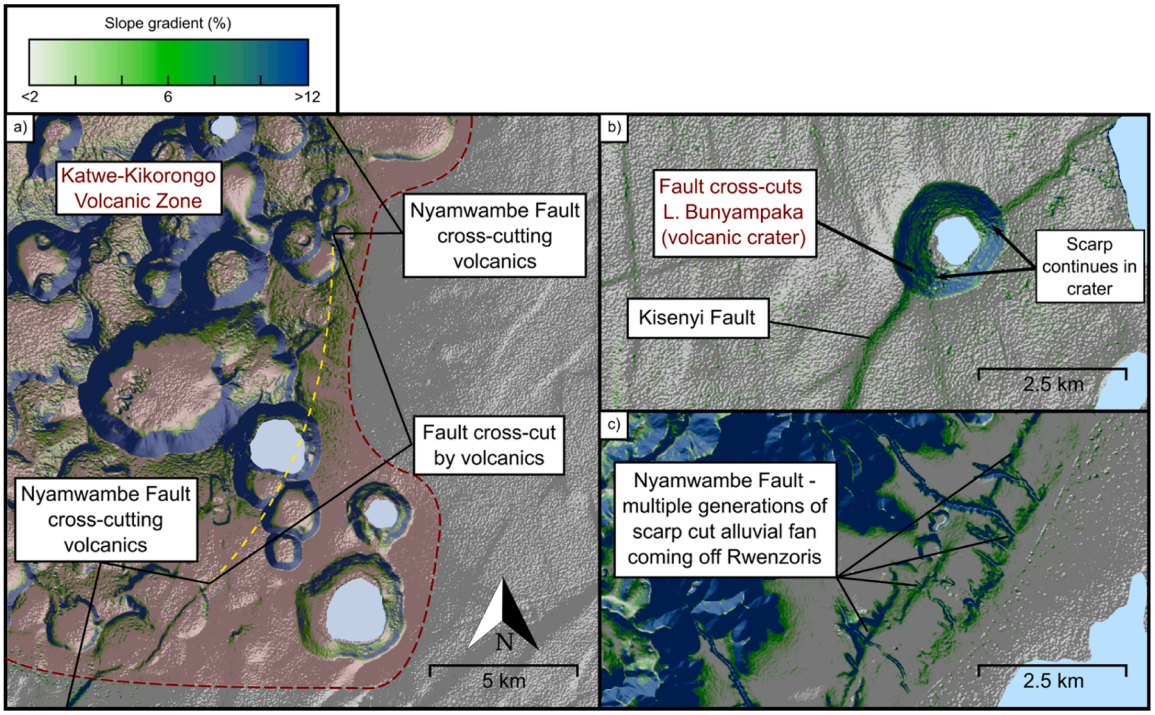

Fig. 4. Slope maps demonstrating the cross-cutting relationships of faults with other Quaternary features. (a) The Nyamwambe Fault (border fault) only partially cross-cuts Katwe-Kikorongo volcanics. (b) The Kisenyi Fault (intrarift fault) cross-cuts the Lake Bunyampaka volcanic crater. (c) The Nyamwambe Fault cross-cuts an alluvial fan – multiple scarps indicate prolonged activity.

repeat measurements have residuals below 0.5 m (Figure S1). Of the 130 faults analysed, 115 had displacement profiles with identifiable first-order patterns. Restricted profiles are the dominant profile-type in the Edward-George Rift (48%) and are split almost evenly between DTR1 (14.8%, symmetric; Fig. 7d), DTR2 (16.5%, asymmetric; Fig. 7e) and DTR3 (16.5%, asymmetric, tip- and half-restricted; Fig. 7f). Restricted profiles are observed throughout the Edward-George Rift, but are most prevalent around the volcanic fields, which are mostly located at the rift margins (Fig. 8a). 33% are unilaterally propagating, and within this 18% are tip-restricted (Fig. 7b) and 15% are half-restricted (Fig. 7c). 7% of fault slip profiles are unrestricted and bilaterally propagating (Fig. 7a). The unilaterally, unrestricted or propagating profiles are mostly clustered around the rift axis, around the Kazinga Channel and Kisenyi Plains (Fig. 8a). The remaining 12% of profiles have an elliptical shape (Fig. 7g-h), although within this group, half the faults (6%) exhibit tapers, which are thought to represent renewed lateral propagation

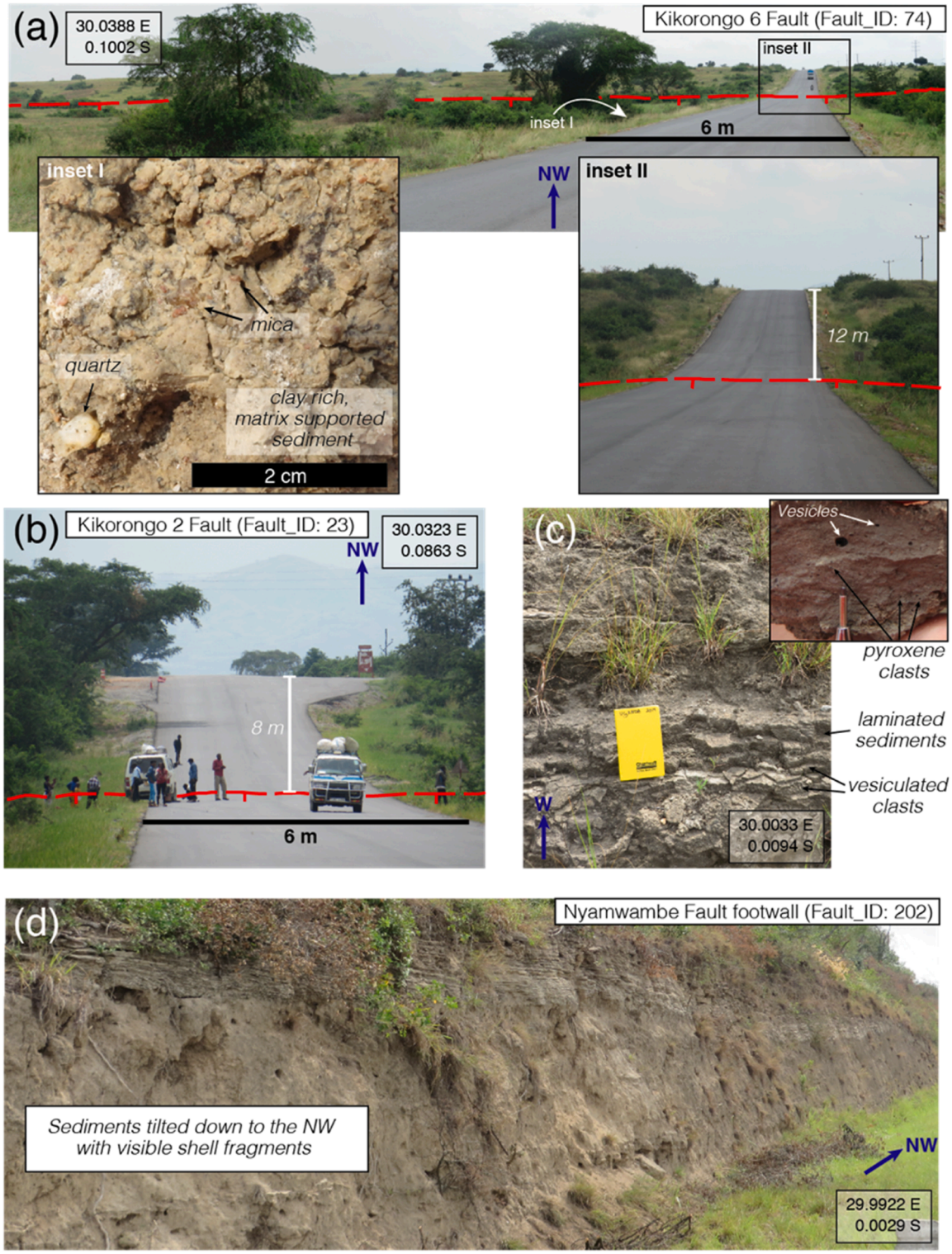

Fig. 5. Field observations from the Edward-George Rift, which were used to verify remote sensing observations. (a) Panoramic view of the Kikorongo 6 fault scarp, an intrarift fault that displaces fine-grained clay rich sediments within the interior of the Edward-George Rift. Inset are (i) views of the hanging wall sediments, and (ii) a zoomed in view of the fault scarp. (b) The fault scarp at the centre of the Kikorongo 2 Fault. (c) Sediments in the hanging wall of the Nyamwambe Fault, proximal to a volcanic crater. Sediments are laminated and with a high number of vesiculated and pyroxene clasts. (d) Sediments in the footwall of the Nyamwambe Fault, tilted away from the fault to the NW, containing shell fragments and ash layers. Figure locations also shown in Figure S2.

following the breaching of a barrier (Manighetti et al., 2001).

In the Edward-George Rift, 54% of faults where we measured the scarp height have a dominant propagation direction. Of these faults, 68% are propagating to the N/NE (Fig. 8b), which is also the direction that the overall rift segment is propagating (Koehn et al., 2010). Only 29% of faults propagate towards the S/SW against the direction of rift propagation, and 3% towards the SE (Fig. 8b). Within these trends, there is a clear spatial division. In the northern half of the region between Lake

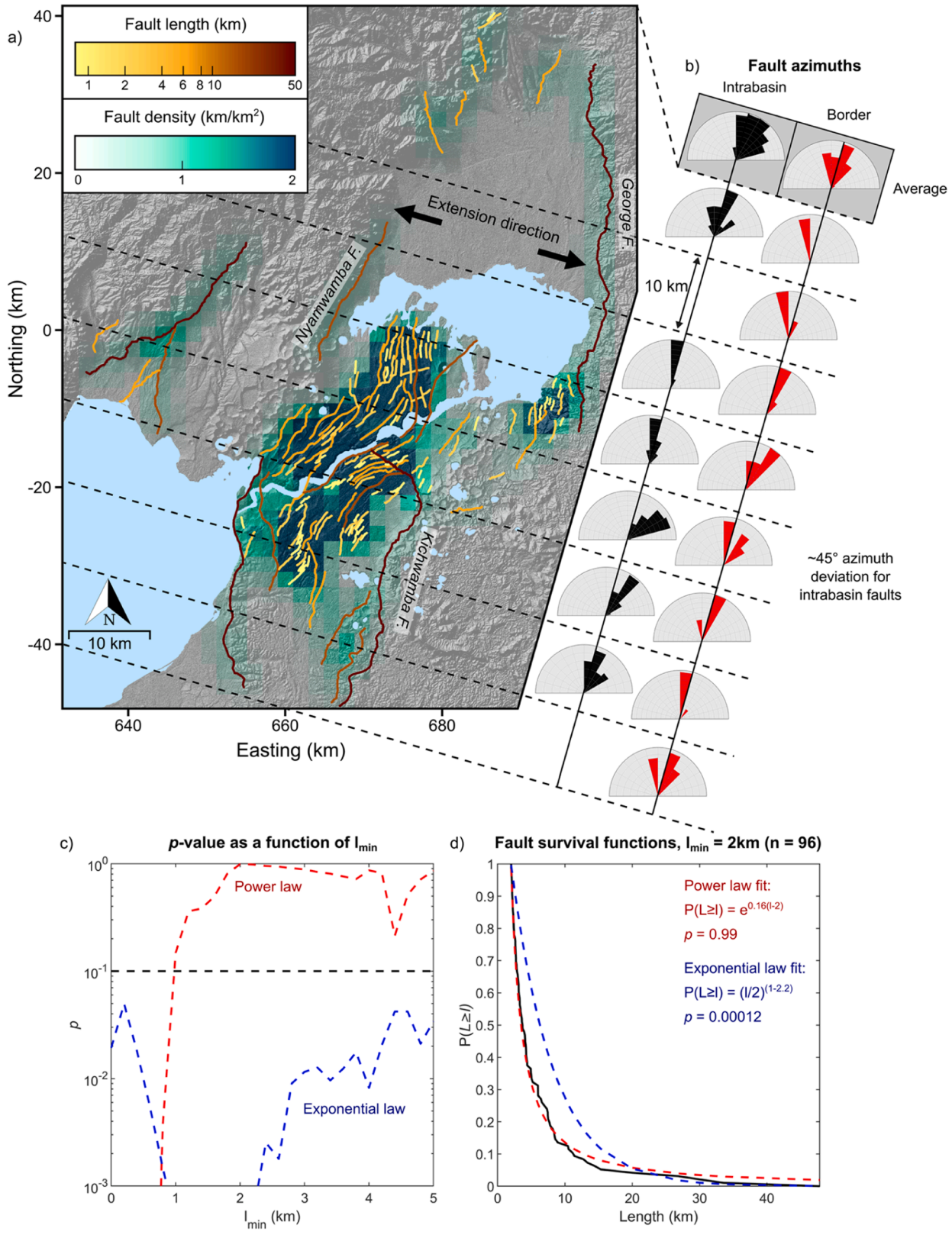

Fig. 6. The density, orientation, and distribution of faults lengths in and adjacent to the Edward-George Rift. (a) The density of faults (in 2 × 2 km^2 boxes) in the Edward-George Rift. (b) Length-weighted rose diagrams showing the fault strike for intrarift and border faults in 10 km intervals perpendicular to the tectonic extension direction (Stamps et al., 2008). (c) Kolmogorov Smirnov (KS) tests used to evaluate p-value as a function of the minimum fault length sampled (l_{min}). Dashed black line signifies the threshold p-value of 0.1. This suggests that l_{min}, the length below which mapping is incomplete, is ~1 km. (d) cCDF (survival) functions for fault lengths over 2 km (to compensate for truncation bias), with power-law and exponential fits.

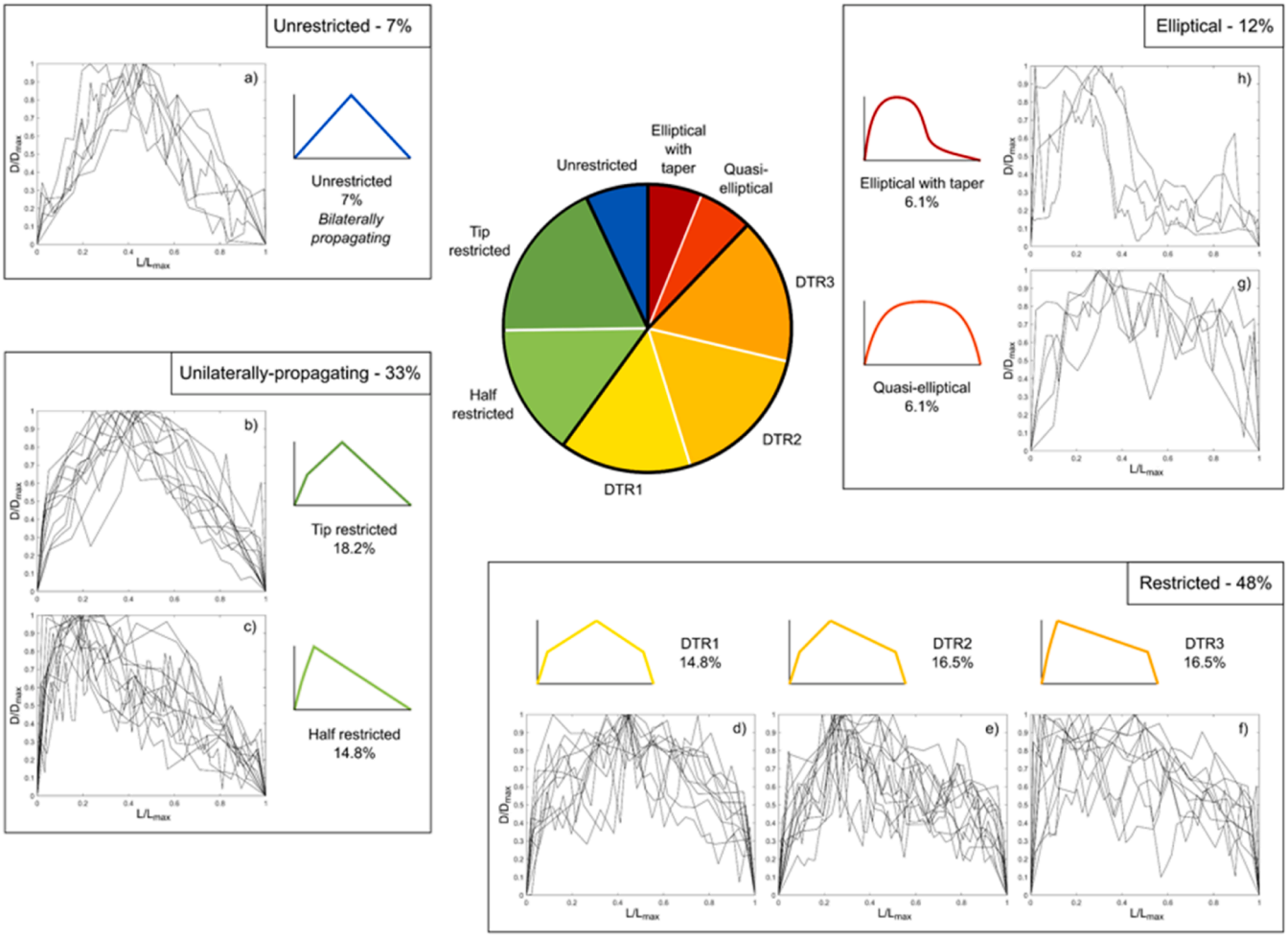

Fig. 7. Distribution of slip profiles for the 115 faults that yielded a clear first order shape, following the classification of Manighetti et al. (2001). Each individual profile has been normalised by its maximum displacement (D_{max}) and length (L_{max}). Profile types are split into groups: those which are unrestricted (a), unilaterally propagating (b-c), restricted (d-f) and elliptical (g-h).

Edward and Lake George, 95% of faults are propagating to the N/NE. In the southern half of this region, only 58% of faults are propagating to the N/NE, with the remaining faults (42%) propagating to the S/SW (Fig. 8b). Throughout the Edward-George Rift, faults generally propagate away from the centre of the volcanic fields, exemplified by a cluster of faults propagating S/SW away from the Katwe-Kikorongo volcanic field (Fig. 8b). At the northern propagating tip of the Lake George basin, propagation trends are more scattered, and 2 faults propagate SE away from the Rwenzori Mountains.

5. Discussion

5.1. Completeness of fault mapping

In total, we mapped 152 active faults in and around the Edward-George Rift and measured the displacement profile of 130 of these faults. 93% (142) are intrarift faults, and 7% (10) are border faults. These faults range in length from 0.8 to 48 km. Although we adopted bias towards inclusiveness when mapping, we emphasise that it is likely that some active faults are missing from our catalogue. This is common in active fault databases worldwide, because some active faults may not have a recognizable surface expression, or may have been buried by sediments or volcanic deposits (see discussions in Williams et al., 2022). Nonetheless, statistical tests of the distribution of fault lengths suggests our map is not necessarily incomplete for faults > 1 km in length. Below, we explore the relative timing of surface faulting and magmatic processes in the Edward-George Rift, the mechanics of how these features form, and then compare these characteristics with other rifts at different stages of evolution.

5.2. Controls on deformation during early magmatic rifting

5.2.1. The relative timing of magmatic rifting and local stress reorientations

Within the Edward-George Rift, volcanic craters are aligned along a NE/SW to NNE/SSW axis (Lærdal and Talbot, 2002), parallel to the orientation of the rift's border faults, and approximately perpendicular to the regional extension direction (106°; Stamps et al., 2008) and the trend of the regional least principal compressive stress (σ_3; 124°; Delvaux and Barth, 2010; Fig. 4& 6). Furthermore, the majority of craters in the region are co-located with the border faults (Fig. 1b and 4a,c). We suggest that these border faults must have formed prior to the rift's magmatism, as it is the elevated permeability around these large displacement fault zones that allows magmatic and hydrothermal fluids to subsequently ascend to the surface (Rowland and Simmons, 2012; Muirhead et al., 2016). This is also consistent with conceptual models for continental rift evolution (Ebinger, 2005).

In contrast to the border fault's ~200 m high escarpments, the Edward-George Rift intrarift faults have no large footwall escarpments (Fig. 1c), and there are fewer volcanic craters in the rift interior than along border faults (Lærdal and Talbot, 2002). Where intrarift faults are co-located with volcanic craters, we observe mutually cross-cutting relationships (Figs. 4 and 5). This indicates that intrarift fault

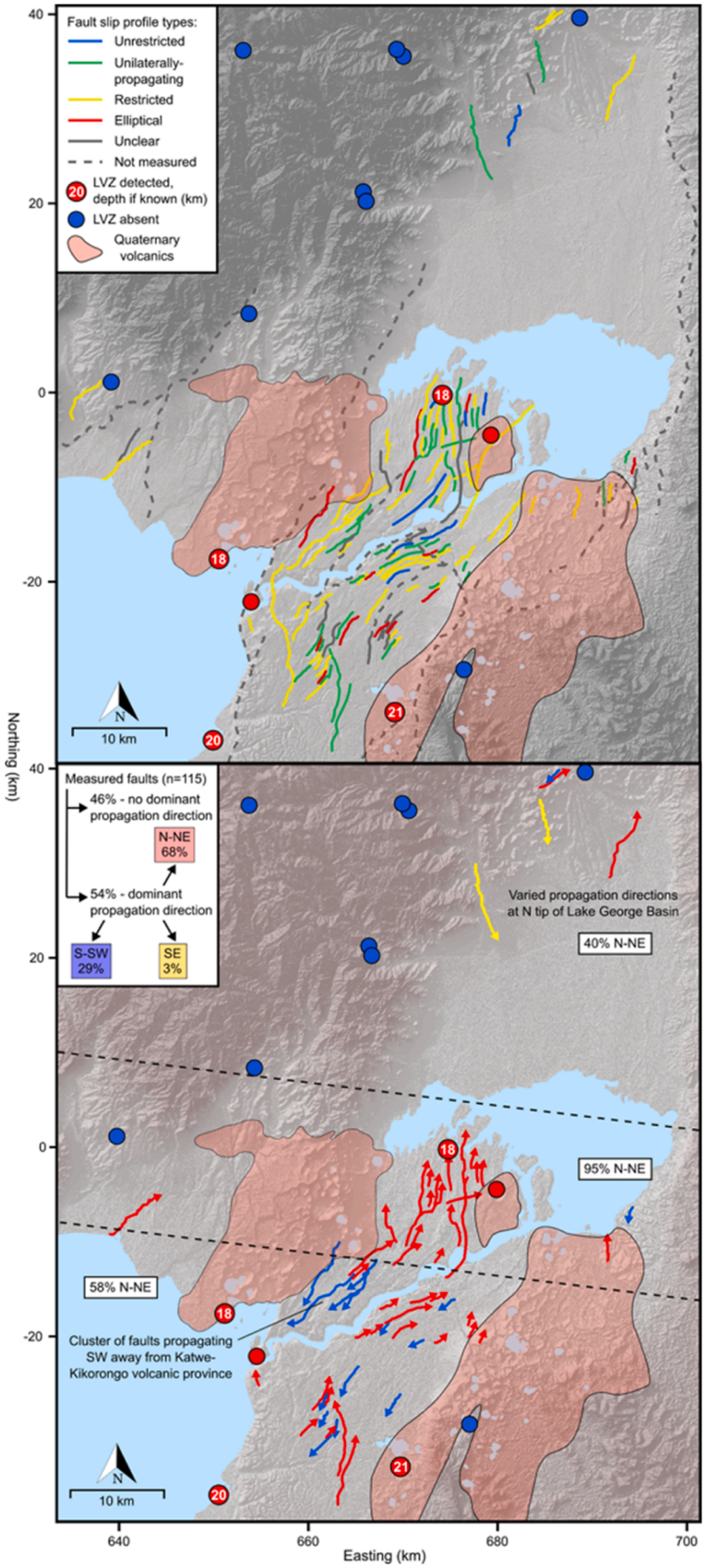

Fig. 8. Topographic maps showing the spatial distribution of (a) slip profile types and (b) fault propagation directions (see text for detail). The extent of Quaternary Toro-Ankole volcanics is modified from Rosenthal et al. (2009). The extent of a mid-crustal LVZ is outlined by seismic stations, shown as red (LVZ detected) and blue (LVZ absent) markers (Wölbern et al., 2010; Gummert et al., 2016).

displacement occurred between deposition of the oldest volcanics and some of the younger volcanics. We cannot discount the possibility that some movement on these intrarift faults also occurred prior to the volcanism and was subsequently buried by the Edward-George Rift's 1–2 km thick package of syn-rift sediments (Upcott et al., 1996). Nevertheless, we surmise that the surface intrarift faults we mapped represents a fault network that has evolved contemporaneously with the volcanism.

Another indicator of the close relationship between the Edward-George Rift's surface intrarift faults and volcanism is that in the vicinity of the rift's magmatic body (as indicated by the mid-crustal low-velocity zone; Figure 1b; Wölbern et al., 2010; Gummert et al., 2016) intrarift fault strike NE-SW to ENE-WSW, whilst the border faults consistently strike NNE-SSW (Fig. 6). Both border and intrarift faults are oblique to the NW-SE striking basement fabrics of the Edward-George Rift (Lærdal and Talbot, 2002; Baglow et al., 2012b). Thus, we exclude the influence of pre-existing structures on intrarift fault orientation, and instead interpret that the intrarift fault azimuth deviations must reflect local rotations in the trend of σ_3. In continental rifts, local stress reorientations can occur due to a range of factors such as intrusion of magmatic bodies, the mechanical influence of interacting faults, and the load from surface topography (including volcanic edifices; e.g. Koehn et al., 2010; Wadge et al., 2016; Hodge et al., 2018; Oliva et al., 2022). Although loading from the growth of the Rwenzori mountains to the east of the Edward-George Rift is thought to have rotated the σ_3 trend since 8 Ma (Koehn et al., 2010), such a regional mechanism cannot explain why only the azimuth of intrarift faults closest to magmatic bodies are deviated (Fig. 6b). We can also discount the influence of volcanic edifice loading on σ_3 rotations in the Edward-George Rift, because of the low relief of maars and volcanic cones and a lack of characteristic radial diking (Muirhead et al., 2015).

Both intrusion and fault interaction can, however, lead to stress rotation in this location (Muirhead et al., 2015; Oliva et al., 2022). Notably, the Edward-George Rift's border faults, which we suggest formed prior to the magmatic rifting, remain orthogonal to the regional extension direction. The magmatic zone is, however, located within a right-step between the George and Kichwamba border faults (Fig. 6), and mechanical interactions between faults may lead to a stress rotation that both influences fault orientations (e.g. Hodge et al., 2018), and leads to local extension that promotes magmatic activity. Once a magmatic system has formed, it can induce a local stress field rotation that also allows new faults to form oblique to the regional stress orientation (Muirhead et al., 2015; Oliva et al., 2022). Thus, local stress reorientation and magmatism are likely interrelated, and both fault interaction and magmatism promote rotations in intrarift fault orientation from the onset of magmatic rifting – the relative importance of these effects is not resolved from current data.

In summary, border fault activity in the Edward-George Rift has been followed by contemporaneous volcanism and intrarift faulting. The transition from border faulting to axial magmatic rifting has been documented in other EARS segments, but over million-year timescales and after significant crustal thinning (Agostini et al., 2011; Muirhead et al., 2016). In the Edward-George Rift, this rift evolution has occurred in the absence of significant crustal thinning (Wölbern et al., 2010), and, given the maximum known age of the Bunyaruguru volcanic field (Pitcavage et al., 2021), possibly within the last 200 kyr.

5.2.2. Changes in crustal strength

Changes in crustal strength can cause changes to the fault density (Zuza et al., 2017) and the b-value of the Gutenberg-Richter earthquake magnitude frequency distribution (Scholz, 2015). In the interior of the Edward George Rift, the fault density is 1-2 km/km^2 (Fig. 6a). This is comparable to fault densities in more evolved EARS magmatic rift segments such as the Main Ethiopian Rift (1-1.6 km/km^2; Agostini et al., 2011), the Dabbahu-Manda-Hararo rift (~2–3 km/km^2; Dumont et al., 2019), which represent the transition between continental rifting and sea-floor spreading, and to mid-ocean ridge segments (1–4 km/km^2; interquartile range of seven spreading centres summarised in Escartín et al., 2014), and it is notably higher than other segments of the Western Branch such as in Malawi (<1 km/km^2; Williams et al., 2022). Our observations from the Edward-George Rift suggest these dense fault networks form at an early stage of magmatic rifting and can persist around the rift axis all the way through the transition to spreading at mid-ocean ridges.

The formation of dense networks of faults are thought to be related to thermo-mechanical changes in crustal strength, although the exact mechanism is not obvious. In general, shorter faults have smaller displacement, and therefore require more faults with smaller spacing to provide a given extension (Cowie and Roberts, 2001). In the Malawi Rift, the low b-value of earthquake aftershock sequences, and the strong, cold crust indicate that the differential stress is generally high (Gaherty et al., 2019; Fagereng et al., 2024). In contrast, the magnitude-frequency distribution of earthquakes in the Edward-George Rift has a high b-value (~1.2; Batte and Rümpker, 2019), which suggests relatively low differential stresses (Scholz, 2015). The activation of more and smaller faults in the Edward-George Rift could therefore be related to the presence of an intrusion allowing faulting at lower stresses and activation of more but smaller structures (Buck, 2004).

The onset of magmatism can lower differential stresses through the injection of melt into the crust and upper mantle, and the exsolution of hydrothermal fluids (Lee et al., 2016). In turn, this is likely to cause spatial variability in the effective stress within the crust, for example reducing effective stress in regions with elevated pore-fluid pressure and increasing tensile stress above propagating dikes (Rowland et al., 2007). Thus, either melt or hydrothermal fluid injection can cause increased fault nucleation, which is thought to have occurred in the Magadi-Natron Rift in Kenya and Tanzania (Muirhead et al., 2016). Furthermore, fluid injection can lead to a cascade of permeability-driven small-magnitude earthquakes (Cox, 2016), which would explain the high b-value and earthquake swarms seen in the Edward-George Rift (Batte and Rümpker, 2019).

If magmatism leads to a lower seismogenic thickness by intruding melt into the brittle crust or raising crustal temperatures (and thus reducing the depth of the frictional-viscous transition), this could also lead to more closely spaced faults by placing a mechanical limit on fault length (Zuza et al., 2017). In relatively slowly extending rifts such as the Edward-George Rift, numerical models indicate that the thermal effects of magmatic intrusions are likely to take millions of years to affect the frictional-viscous transition within the crust (Daniels et al., 2014). However, we note that there are fewer earthquakes between 15 and 25 km depth beneath the Edward-George Rift compared with other areas of the Albertine Rift (Lindenfeld et al., 2012), the depth at which a low-velocity zone has been interpreted as the effect of a zone of partial melt within the crust (Wölbern et al., 2010). This implies that the thermal effects of magmatic intrusions may occur on shorter timescales than suggested by previous numerical models.

5.2.3. Influences on fault slip profiles

A high number of asymmetric and tip restricted fault slip profiles are a feature of magmatic rift segments (Figure 7; Table 1; Manighetti et al., 2001; Dumont et al., 2017). Asymmetric profiles with a single propagation direction or one/both of their tips restricted for growth (unilateral, restricted or elliptical with taper profiles in Fig. 3) dominate in magmatic rift segments in East Africa (Table 1), representing 87% of faults in the Edward-George Rift, 83.5% of faults in the Dabbahu-Manda-Hararo Rift (DMHR), and 68% of faults in the Asal-Ghoubbet-Afar Rift (AGAR) (Manighetti et al., 2001; Dumont et al., 2017). We are unable to compare these with faults in well-studied amagmatic rifts, as these are now mostly growing through segment linkage which obscures their first-order fault-slip profiles (e.g. Wedmore et al., 2020). Asymmetric and non-elliptical fault slip distributions can be caused by a range of factors including stress gradients in the crust,

Table 1
Comparison of fault slip profile classifications for different magmatic rift segments in East Africa given as percentages.

Region	Unrestricted	Unilaterally propagating			Elliptical			Restricted				Number of faults	Source
	Total	Tip Restricted	Half restricted	Total	Elliptical with taper	Quasi-elliptical	Total	DTR1	DTR2	DTR3	Total		
Edward-George Rift	7	18.2	14.8	33	6.1	6.1	12.2	14.8	16.5	16.5	47.8	115	This paper
Dabbahu-Manda-Harraro Rift	4.2	7.6	14.8	22.4	17.4	12.3	29.7	3.1	11.5	29.1	43.7	357	Dumont et al., 2017
Asal Rift	5	14	30	44	-a	24	24	6	1	12	19	94[c]	Manighetti et al., 2001
Ghoubbet Rift	0	8	34	42	-a	5.5	5.5	8	2.7	19	29.7	40[c]	Manighetti et al., 2001
Afar Rift	5	18	17.5	35.5	-a	12.5	12.5	2.5	9.2	22.5	34.2	121[c]	Manighetti et al., 2001
Asal-Ghoubbet-Afar Riftb	4	15.5	24	39.5	-a	15.4	15.4	4.6	5.4	18.3	28.3	240[c]	Manighetti et al., 2001

[a] – no totals provided for this classification, as remaining% of faults were classified as having an intermediate shape.
[b] – results aggregated from the three rifts above.
[c] – the numbers from the three individual rifts do not add up to the total number of faults analysed, as 15 faults could not be classified, but the breakdown by individual rift was not provided.

heterogeneous elastic material parameters, inelastic deformation (especially at fault tips) and mechanical interaction between faults (Bürgmann et al., 1994). Isolating the influence of any one of these factors is challenging; however, we explore below the possible impact of intrusions on these slip profiles, as this factor as this is unique to magmatic rifts.

5.3. Competing tectonic and magmatic controls on fault growth and propagation

Fault propagation in the Edward-George Rift shows a mixed signal of both tectonic and magmatic influences. Of the faults we mapped that show a dominant propagation direction, 68% of faults propagate to the N/NE (Fig. 8b), in the direction of long-term rift propagation (Lindenfeld et al., 2012). To the northeast of the mid-crustal magmatic body, 95% of faults propagate N/NE, away from the magmatic body and in the direction of rift propagation. To the southwest of the magmatic body, 58% of faults propagate to the N/NE with the overall rift propagation direction whereas 42% of faults propagate S/SW away from the magmatic body. Therefore, both rift propagation and magmatic bodies influence the propagation direction in the Edward-George Rift demonstrating a mixed tectonic-magmatic influence.

In the magma-rich Dabbahu-Manda-Hararo rift, it has been suggested that fault propagation direction can be used to track the presence and migration of crustal magmatic bodies (Dumont et al., 2017). Our research suggests that in the initial stages of magmatic rifting this approach may not always yield reliable results as both regional tectonics and local magmatic processes affect fault growth. However, a comparison of the distribution of fault lengths in the Edward-George Rift with three other well-mapped publicly available fault maps from other segments of the EARS suggests the influence of magmatism on fault growth is established rapidly then changes progressively through time (Fig. 9). In the magma-poor Malawi Rift, long faults take up most of the regional extension (Wedmore et al., 2020), and the distribution of fault lengths is best fit by a power-law with an exponent of 1.9 ± 0.2 (Figure 9; Williams et al., 2022). Conversely, in the magma-rich Northern Main Ethiopian Rift and Dabbahu-Manda-Hararo Rift, where diking accommodates 80% of the extension at depth and normal faults accommodate larger than usual horizontal displacements (Rowland et al., 2007), deformation is taken up across a network of closely spaced short faults with a greater power-law exponent (3.2 ± 0.4 for the Dabbahu-Manda-Hararo rift, 3.3 ± 0.3 for the Wonji Fault Belt in the Northern Main Ethiopian Rift, Figure S3, S4 and 9; Agostini et al., 2011; Dumont et al., 2017). In the Edward-George Rift, which is at the earliest stages of magmatic rifting,

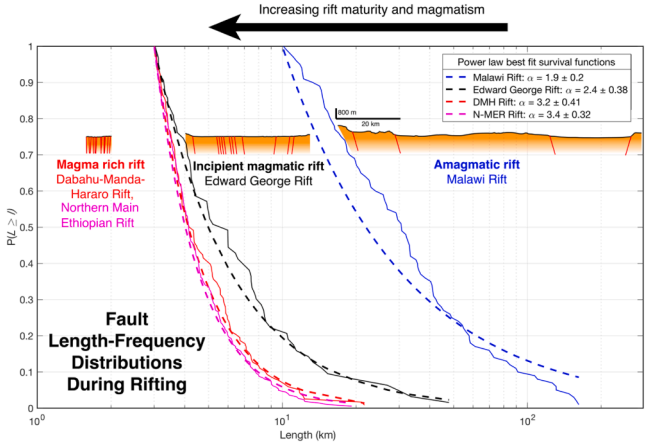

Fig. 9. Comparison of fault length distributions along the EARS. For each fault system, empirical and power law complementary cumulative frequency (survival) distributions are shown with l_{min} of 3 km for the Dabbahu-Manda-Hararo rift (Figure S3; Dumont et al., 2017), Wonji Fault Belt in the Northern Main Ethiopian Rift (N-MER, Figure S4; Agostini et al., 2011), and Edward George Rifts, and l_{min} of 10 km for the Malawi Rift (Williams et al., 2022). The power law exponent (α) for each rift's fault length distribution is also reported and indicates that as rifts evolve from amagmatic to magma-rich rifting, α increases as the fault systems become dominated by shorter faults. Example cross sections of the Dabbahu-Manda-Hararo, Edward-George, and Malawi rifts are also plotted at the same scale and at four times vertical exaggeration.

fault lengths occupy an intermediate state, with the majority of faults <10 km in length, but with a smaller power law exponent of 2.4 ± 0.4 (Figs 7d & 9). Thus, as rifts transition from magma-poor to magma-rich the fault system rapidly changes from one dominated by long segmented faults with lower power-law exponents, to one dominated by closely spaced short faults with higher power law-exponents (Fig. 9). However, at some critical fault density, the fault network is expected to saturate, leading to an exponential frequency-size distribution and large displacement:length ratios (Gupta and Scholz, 2000).

6. Conclusions and implications

We used high-resolution TanDEM-X topography to map 152 active normal fault scarps in the Edward-George Rift in Uganda. We systematically compiled the attributes of each fault in a freely available active

fault database, and where possible measured the along-strike displacement profile of each fault. Our three main conclusions regarding how and when the characteristic properties of magmatic rifts first form are:

1) Initial volcanism is restricted mainly to the edges of the rift, with magmatic fluids appearing to flow along large-offset border faults. The onset of volcanism reduces the overall bulk strength of the crust and a contemporaneous dense network of short faults with asymmetric fault displacement profiles forms in the rift interior. We suggest development of this fault network is facilitated by magma intrusion into the crust, and the release of magmatic volatiles which cause: i) a decrease in the differential stress that can be sustained within the upper crust; ii) a decrease in the effective stress; and iii) and elevation of the frictional/viscous transition.
2) Despite the initial rapid increase in the influence of magmatism on the growth and distribution of active faults, regional tectonics still matters. In the Edward-George Rift, the location of the border faults controls the initial ascent path of magmatic fluids, and magma is confined to intrabasin accommodation zones. Fault propagation direction is also affected by regional tectonics, but there is also a notable signal whereby a large number of faults propagate away from the centre of a mid-crustal magmatic body.
3) In amagmatic rifts, fault networks are initially dominated by long faults. At the onset of magmatism, the crust weakens and the fault network transitions to one with a high frequency of closely-spaced short faults that accommodate deformation at the rift axis (although some deformation at the rift margins persists). A high fault density network with an abundance of short faults then persists as the lithosphere thins and the volume of magma intruded into the crust increases and is still present in fault systems at mid-ocean ridge segments.

Data availability

The geospatial database of fault traces and scarp heights is freely available and open source, under a Creative Commons CC-BY-4.0 licence. The database can be accessed on the Zenodo Data Archive (DOI: https://doi.org/10.5281/zenodo.6510002) in a variety of file formats to ensure compatibility with various software packages. The version of record is plain text, human readable GeoJSON format, however it is also available in ESRI shapefile and KML formats.

CRediT authorship contribution statement

Luke N.J. Wedmore: Conceptualization, Formal analysis, Investigation, Methodology, Project administration, Supervision, Writing – original draft, Writing – review & editing. **Dan Evans:** Data curation, Formal analysis, Investigation, Writing – original draft. **Jack N. Williams:** Conceptualization, Investigation, Writing – review & editing. **Juliet Biggs:** Funding acquisition, Investigation, Project administration, Supervision, Writing – review & editing. **Åke Fagereng:** Writing – review & editing, Supervision, Funding acquisition, Conceptualization. **Peter Mawejje:** Resources, Investigation. **Fred Tugume:** Investigation, Conceptualization. **Thomas Blenkinsop:** Writing – review & editing, Funding acquisition, Conceptualization. **Daniel E.J. Hobley:** Writing – review & editing, Funding acquisition, Conceptualization.

Declaration of competing interest

The authors declare that they have no known competing financial interests or personal relationships that could have appeared to influence the work reported in this paper.

Acknowledgements

This manuscript originated as a University of Bristol MSci project conducted by Dan Evans. The overall project was funded by EPSRC Global Challenges Research Fund PREPARE (EP/P028233/1), SAFER PREPARE (part of the Innovative data services for aquaculture, seismic resilience, and drought adaptation in East Africa grant; EP/T015462/1), and EPSRC IAA award from University of Bristol and Cardiff University. TanDEM-X data were obtained via DLR proposal DEM_GEOL2737. Stéphanie Dumont kindly provided us with the Afar fault data analysed in Figure S3. Geological maps were provided by the Uganda Department of Geological Survey and Mines (Baglow et al., 2012a/b). We thank James Muirhead and Stéphanie Dumont for their constructive reviews of this manuscript.

Supplementary materials

Supplementary material associated with this article can be found, in the online version, at doi:10.1016/j.epsl.2024.118762.

References

Ackermann, R.V., Schlische, R.W., Withjack, M.O., 2001. The geometric and statistical evolution of normal fault systems: An experimental study of the effects of mechanical layer thickness on scaling laws. J. Struct. Geol. (23), 1803–1819. https://doi.org/10.1016/S0191-8141(01)00028-1 v.

Agostini, A., Bonini, M., Corti, G., Sani, F., Mazzarini, F., 2011. Fault architecture in the Main Ethiopian Rift and comparison with experimental models: Implications for rift evolution and Nubia-Somalia kinematics. Earth. Planet. Sci. Lett. 301, 479–492. https://doi.org/10.1016/j.epsl.2010.11.024 v.

Baglow, N., et al., 2012a. Geological Map of Uganda, Mineral Potential areas, Sheet SA-36-1 (Mbarara),, 1:250,000.

Baglow, N. et al., 2012b, Geological map of Uganda, mineral potential areas, shet NA-36-13 (Fort Portal), 1:250000.

Batte, A.G., Rümpker, G., 2019. Spatial mapping of b-value heterogeneity beneath the Rwenzori region, Albertine rift: Evidence of magmatic intrusions. Journal of Volcanology and Geothermal Research 381, 238–245. https://doi.org/10.1016/j.jvolgeores.2019.05.015 v.

Biggs, J., Ayele, A., Fischer, T.P., Fontijn, K., Hutchison, W., Kazimoto, E., Whaler, K., Wright, T.J., 2021. Volcanic activity and hazard in the East African Rift Zone. Nat. Commun. 12, 6881. https://doi.org/10.1038/s41467-021-27166-y v.

Boven, A., Pasteels, P., Punzalan, L.E., Yamba, T.K., Musisi, J.H., 1998. Quaternary perpotassic magmatism in Uganda (Toro-Ankole Volcanic Province): age assessment and significance for magmatic evolution along the East African Rift. Journal of African Earth Sciences 26, 463–476. https://doi.org/10.1016/s0899-5362(98)00026-8 v.

Bubeck, A., Walker, R.J., Imber, J., MacLeod, C.J., 2018. Normal fault growth in layered basaltic rocks: The role of strain rate in fault evolution. J. Struct. Geol. 115, 103–120. https://doi.org/10.1016/j.jsg.2018.07.017 v.

Buck, W.R., 2004. Consequences of Asthenospheric Variability on Continental Rifting. Rheology and Deformation of the Lithosphere at Continental Margins, pp. 1–30. https://doi.org/10.7312/karn12738-002.

Bürgmann, R., Pollard, D.D., Martel, S.J., 1994. Slip distributions on faults: effects of stress gradients, inelastic deformation, heterogeneous host-rock stiffness, and fault interaction. J. Struct. Geol. 16, 1675–1690. https://doi.org/10.1016/0191-8141(94)90134-1 v.

Cartwright, J.A., Trudgill, B.D., Mansfield, C.S., 1995. Fault growth by segment linkage: an explanation for scatter in maximum displacement and trace length data from the Canyonlands Grabens of SE Utah. J. Struct. Geol. 17, 1319–1326. https://doi.org/10.1016/0191-8141(95)00033-A v.

Cowie, P.A., 1998. A healing-reloading feedback control on the growth rate of seismogenic faults. J. Struct. Geol. 20, 1075–1087. https://doi.org/10.1016/S0191-8141(98)00034-0 v.

Cowie, P.A., Roberts, G.P., 2001. Constraining slip rates and spacings for active normal faults. J. Struct. Geol. (23), 1901–1915. https://doi.org/10.1016/S0191-8141(01)00036-0 v.

Cowie, P.A., Scholz, C.H., Edwards, M., Malinverno, A., 1993. Fault strain and seismic coupling on mid-ocean ridges. Journal of Geophysical Research: Solid Earth 98, 17911–17920. https://doi.org/10.1029/93JB01567 v.

Cox, S.F., 2016. Injection-Driven Swarm Seismicity and Permeability Enhancement: Implications for the Dynamics of Hydrothermal Ore Systems in High Fluid-Flux, Overpressured Faulting Regimes—An Invited Paper. Economic Geology 111, 559–587. https://doi.org/10.2113/econgeo.111.3.559 v.

Daniels, K.A., Bastow, I.D., Keir, D., Sparks, R.S.J., Menand, T., 2014. Thermal models of dyke intrusion during development of continent–ocean transition. Earth. Planet. Sci. Lett. 385, 145–153. https://doi.org/10.1016/j.epsl.2013.09.018 v.

Delcamp, A., Mossoux, S., Belkus, H., Tweheyo, C., Mattsson, H.B., Kervyn, M., 2019. Control of the stress field and rift structures on the distribution and morphology of explosive volcanic craters in the Manyara and Albertine rifts. Journal of African Earth Sciences 150, 566–583. https://doi.org/10.1016/j.jafrearsci.2018.09.012 v.

Delvaux, D., Barth, A., 2010. African stress pattern from formal inversion of focal mechanism data. Tectonophysics. 482, 105–128. https://doi.org/10.1016/j.tecto.2009.05.009 v.

Dumont, S., Klinger, Y., Socquet, A., Doubre, C., Jacques, E., 2017. Magma influence on propagation of normal faults: Evidence from cumulative slip profiles along Dabbahu-Manda-Hararo rift segment (Afar, Ethiopia). J. Struct. Geol. 95, 48–59. https://doi.org/10.1016/j.jsg.2016.12.008 v.

Dumont, S., Klinger, Y., Socquet, A., Escartín, J., Grandin, R., Jacques, E., Medynski, S., Doubre, C., 2019. Rifting Processes at a Continent-Ocean Transition Rift Revealed by Fault Analysis: Example of Dabbahu-Manda-Hararo Rift (Ethiopia). Tectonics. 38, 190–214. https://doi.org/10.1029/2018TC005141 v.

Ebinger, C., 2005. Continental break-up: The East African perspective. Astronomy and Geophysics 46, 2.16–2.21. https://doi.org/10.1111/j.1468-4004.2005.46216.x v.

Ebinger, C.J., 1989. Tectonic Development of the Western Branch of the East African Rift System, 101. Geological Society of America Bulletin, pp. 885–903. https://doi.org/10.1130/0016-7606(1989)101<0885:TDOTWB>2.3.CO;2 v.

Ebinger, C.J., Casey, M., 2001. Continental breakup in magmatic provinces: An Ethiopian example: Geology, v. 29 527–530. https://doi.org/10.1130/0091-7613(2001)029<0527:CBIMPA>2.0.CO;2.

Escartín, J., Soule, S.A., Cannat, M., Fornari, D.J., Düşünür, D., Garcia, R., 2014. Lucky Strike seamount: Implications for the emplacement and rifting of segment-centered volcanoes at slow spreading mid-ocean ridges: Geochemistry, Geophysics. Geosystems 15, 4157–4179. https://doi.org/10.1002/2014GC005477 v.

Fagereng, Diener, J.F.A., Tulley, C.J., Manda, B., 2024. Metamorphic Inheritance, Lower-Crustal Earthquakes, and Continental Rifting: Geochemistry, Geophysics. Geosystems 25. https://doi.org/10.1029/2023GC011305 v.

Gaherty, J.B., et al., 2019. Faulting processes during early-stage rifting: Seismic and geodetic analysis of the 2009-2010 Northern Malawi earthquake sequence. Geophysical Journal International, v 217, 1767–1782. https://doi.org/10.1093/gji/ggz119.

Gummert, M., Lindenfeld, M., Wölbern, I., Rümpker, G., Celestin, K., Batte, A., 2016. Crustal Structure and High-Resolution Moho topography Across the Rwenzori region (Albertine rift) from P-receiver functions: Geological Society, 420. Special Publications, London, pp. 69–82. https://doi.org/10.1144/SP420.4 v.

Gupta, A., Scholz, C.H., 2000. Brittle strain regime transition in the Afar depression: Implications for fault growth and seafloor spreading. Geology. 28, 1087–1090. https://doi.org/10.1130/0091-7613(2000)28<1087:BSRTIT>2.0.CO v.

Hodge, M., Fagereng, A., Biggs, J., 2018. The Role of Coseismic Coulomb Stress Changes in Shaping the Hard Link Between Normal Fault Segments. Journal of Geophysical Research: Solid Earth (123), 797–814. https://doi.org/10.1002/2017JB014927 v.

Illsley-Kemp, F., Savage, M.K., Keir, D., Hirschberg, H.P., Bull, J.M., Gernon, T.M., Hammond, J.O.S., Kendall, J.M., Ayele, A., Goitom, B., 2017. Extension and stress during continental breakup: Seismic anisotropy of the crust in Northern Afar. Earth. Planet. Sci. Lett. 477, 41–51. https://doi.org/10.1016/j.epsl.2017.08.014 v.

Jess, S., Koehn, D., Fox, M., Enkelmann, E., Sachau, T., Aanyu, K., 2020. Paleogene initiation of the Western Branch of the East African Rift: The uplift history of the Rwenzori Mountains, Western Uganda. Earth and Planetary Science Letters, v 552. https://doi.org/10.1016/j.epsl.2020.116593.

Kendall, J.M., Stuart, G.W., Ebinger, C.J., Bastow, I.D., Keir, D., 2005. Magma-assisted rifting in Ethiopia. Nature 433, 146–148. https://doi.org/10.1038/nature03161 v.

Kinabo, B.D., Hogan, J.P., Atekwana, E.A.E.A., Abdelsalam, M.G., Modisi, M.P., 2008. Fault growth and propagation during incipient continental rifting: Insights from a combined aeromagnetic and Shuttle Radar Topography Mission digital elevation model investigation of the Okavango Rift Zone, northwest Botswana. Tectonics. 27, 1–16. https://doi.org/10.1029/2007TC002154 v.

King, G., 1983. The accommodation of large strains in the upper lithosphere of the earth and other solids by self-similar fault systems: the geometrical origin of b-Value. Pure and Applied Geophysics PAGEOPH 121, 761–815. https://doi.org/10.1007/BF02590182 v.

Koehn, D., Lindenfeld, M., Rümpker, G., Aanyu, K., Haines, S., Passchier, C.W., Sachau, T., 2010. Active transsection faults in rift transfer zones: Evidence for complex stress fields and implications for crustal fragmentation processes in the western branch of the East African Rift. International Journal of Earth Sciences 99, 1633–1642. https://doi.org/10.1007/s00531-010-0525-2 v.

Koehn, D., Steiner, A., Aanyu, K., 2019. Modelling of extension and dyking-induced collapse faults and fissures in rifts. J. Struct. Geol. 118, 21–31. https://doi.org/10.1016/j.jsg.2018.09.017 v.

Lærdal, T., Talbot, M.R., 2002. Basin neotectonics of lakes Edward and George, East African Rift. Palaeogeogr. Palaeoclimatol. Palaeoecol. 187, 213–232. https://doi.org/10.1016/S0031-0182(02)00478-9 v.

Lee, H., Muirhead, J.D., Fischer, T.P., Ebinger, C.J., Kattenhorn, S.A., Sharp, Z.D., Kianji, G., 2016. Massive and prolonged deep carbon emissions associated with continental rifting. Nat. Geosci. (9), 145–149. https://doi.org/10.1038/ngeo2622 v.

Lindenfeld, M., Rümpker, G., Link, K., Koehn, D., Batte, A., 2012. Fluid-triggered earthquake swarms in the Rwenzori region, East African Rift-Evidence for rift initiation. Tectonophysics. 566–567, 95–104. https://doi.org/10.1016/j.tecto.2012.07.010 v.

Manighetti, I., King, G.C.P., Gaudemer, Y., Scholz, C.H., Doubre, C., 2001. Slip accumulation and lateral propagation of active normal faults in Afar. Journal of Geophysical Research: Solid Earth 106, 13667–13696. https://doi.org/10.1029/2000JB900471 v.

McGlue, M.M., Scholz, C.a., Karp, T., Ongodia, B., Lezzar, K.E., 2006. Facies Architecture of Flexural Margin Lowstand Delta Deposits in Lake Edward, East African Rift. Journal of Sedimentary Research 76, 942–958. https://doi.org/10.2110/jsr.2006.068 v.

Muirhead, J.D., Kattenhorn, S.A., Le Corvec, N., 2015. Varying styles of magmatic strain accommodation across the East African Rift. Geochemistry, Geophysics, Geosystems 16, 2775–2795. https://doi.org/10.1002/2015GC005918 v.

Muirhead, J.D., Kattenhorn, S.A., Lee, H., Mana, S., Turrin, B.D., Fischer, T.P., Kianji, G., Dindi, E., Stamps, D.S., 2016. Evolution of upper crustal faulting assisted by magmatic volatile release during early-stage continental rift development in the East African Rift. Geosphere 12, 1670–1700. https://doi.org/10.1130/GES01375.1 v.

Muirhead, J.D., Wright, L.J.M., Scholz, C.A., 2019. Rift evolution in regions of low magma input in East Africa. Earth. Planet. Sci. Lett. 506, 332–346. https://doi.org/10.1016/j.epsl.2018.11.004 v.

Njinju, E.A., Atekwana, E.A., Stamps, D.S., Abdelsalam, M.G., Atekwana, E.A., Mickus, K.L., Fishwick, S., Kolawole, F., Rajaonarison, T.A., Nyalugwe, V.N., 2019. Lithospheric Structure of the Malawi Rift: Implications for Magma-Poor Rifting Processes. Tectonics. 38, 3835–3853. https://doi.org/10.1029/2019TC005549 v.

Oliva, S.J., Ebinger, C.J., Rivalta, E., Williams, C.A., Wauthier, C., Currie, C.A., 2022. State of stress and stress rotations: Quantifying the role of surface topography and subsurface density contrasts in magmatic rift zones (Eastern Rift, Africa). Earth and Planetary Science Letters, v 584, 117478. https://doi.org/10.1016/j.epsl.2022.117478.

Pitcavage, E., Furman, T., Nelson, W.R., Kalegga, P.K., Barifaijo, E., 2021. Petrogenesis of primitive lavas from the Toro Ankole and Virunga Volcanic Provinces: Metasomatic mineralogy beneath East Africa's Western Rift. Lithos. 396–397, 106192 https://doi.org/10.1016/j.lithos.2021.106192 v.

Plasman, M., Tiberi, C., Ebinger, C., Gautier, S., Albaric, J., Peyrat, S., Déverchère, J., Le Gall, B., Tarits, P., Roecker, S., 2017. Lithospheric low-velocity zones associated with a magmatic segment of the Tanzanian Rift, East Africa. Geophys. J. Int. 210, 465–481 v.

Rosenthal, A., Foley, S.F., Pearson, D.G., Nowell, G.M., Tappe, S., 2009. Petrogenesis of strongly alkaline primitive volcanic rocks at the propagating tip of the western branch of the East African Rift. Earth. Planet. Sci. Lett. 284, 236–248 v.

Rotevatn, A., Jackson, C.A.L., Tvedt, A.B.M., Bell, R.E., Blækkan, I., 2019. How do normal faults grow? J. Struct. Geol. 125, 174–184. https://doi.org/10.1016/j.jsg.2018.08.005 v.

Rowland, J.V., Baker, E., Ebinger, C.J., Keir, D., Kidane, T., Biggs, J., Hayward, N., Wright, T.J., 2007. Fault growth at a nascent slow-spreading ridge: 2005 Dabbahu rifting episode, Afar. Geophys. J. Int. 171, 1226–1246. https://doi.org/10.1111/j.1365-246X.2007.03584.x v.

Rowland, J.V., Simmons, S.F., 2012. Hydrologic, Magmatic, and Tectonic Controls on Hydrothermal Flow, Taupo Volcanic Zone, New Zealand: Implications for the Formation of Epithermal Vein Deposits. Economic Geology 107, 427–457. https://doi.org/10.2113/econgeo.107.3.427 v.

Samsu, A., Micklethwaite, S., Williams, J.N., Fagereng, Å., Cruden, A.R., 2023. Structural inheritance in amagmatic rift basins: Manifestations and mechanisms for how pre-existing structures influence rift-related faults. Earth. Sci. Rev. 246, 104568 https://doi.org/10.1016/j.earscirev.2023.104568 v.

Scholz, C.H., 2015. On the stress dependence of the earthquake b value. Geophys. Res. Lett. 42, 1399–1402. https://doi.org/10.1002/2014GL062863 v.

Shaw, P.R., 1992. Ridge segmentation, faulting and crustal thickness in the Atlantic Ocean. Nature 358, 490–493. https://doi.org/10.1038/358490a0 v.

Simon, B., Guillocheau, F., Robin, C., Dauteuil, O., Nalpas, T., Pickford, M., Senut, B., Lays, P., Bourges, P., Bez, M., 2017. Deformation and sedimentary evolution of the Lake Albert Rift (Uganda, East African Rift System). Mar. Pet. Geol. 86, 17–37. https://doi.org/10.1016/j.marpetgeo.2017.05.006 v.

Stamps, D.S., Calais, E., Saria, E., Hartnady, C., Nocquet, J.M., Ebinger, C.J., Fernandes, R.M., 2008. A kinematic model for the East African Rift. Geophys. Res. Lett. 35 https://doi.org/10.1029/2007GL032781 v.

Stamps, D.S., Kreemer, C., Fernandes, R., Rajaonarison, T.A., Rambolamanana, G., 2021. Redefining East African Rift System kinematics. Geology. 49, 150–155. https://doi.org/10.1130/G47985.1 v.

Sun, M., Gao, S.S., Liu, K.H., Mickus, K., Fu, X., Yu, Y., 2021. Receiver function investigation of crustal structure in the Malawi and Luangwa rift zones and adjacent areas. Gondwana Research 89, 168–176. https://doi.org/10.1016/j.gr.2020.08.015 v.

Temtime, T., Biggs, J., Lewi, E., Ayele, A., 2020. Evidence for Active Rhyolitic dike Intrusion in the Northern Main Ethiopian Rift from the 2015 Fentale Seismic Swarm. Geochemistry, Geophysics, Geosystems 21. https://doi.org/10.1029/2019GC008550 v.

Upcott, N.M., Mukasa, R.K., Ebinger, C.J., Karner, G.D., 1996. Along-axis segmentation and isostasy in the Western rift, East Africa. Journal of Geophysical Research: Solid Earth 101, 3247–3268. https://doi.org/10.1029/95jb01480 v.

Wadge, G., Biggs, J., Lloyd, R., Kendall, J.M., 2016. Historical Volcanism and the State of Stress in the East African Rift System. Front. Earth. Sci. (Lausanne) (4). https://doi.org/10.3389/feart.2016.00086 v.

Wedmore, L.N.J., Biggs, J., Floyd, M., Fagereng, Mdala, H., Chindandali, P., Williams, J.N., Mphepo, F., 2021. Geodetic Constraints on Cratonic Microplates and Broad Strain During Rifting of Thick Southern African Lithosphere. Geophys. Res. Lett. 48. https://doi.org/10.1029/2021GL093785 v.

Wedmore, L.N.J., Biggs, J., Williams, J.N., Fagereng, Å., Dulanya, Z., Mphepo, F., Mdala, H., 2020. Active Fault Scarps in Southern Malawi and Their Implications for the Distribution of Strain in Incipient Continental Rifts. Tectonics. 39, e2019TC005834 https://doi.org/10.1029/2019TC005834 v.

Wessel, B., Huber, M., Wohlfart, C., Marschalk, U., Kosmann, D., Roth, A., 2018. Accuracy assessment of the global TanDEM-X Digital Elevation Model with GPS data. ISPRS Journal of Photogrammetry and Remote Sensing 139, 171–182 v.

White, R., McKenzie, D., 1989. Magmatism at rift zones: The generation of volcanic continental margins and flood basalts. J. Geophys. Res. 94, 7685. https://doi.org/10.1029/JB094iB06p07685 v.

Williams, J.N., et al., 2022. The Malawi Active Fault Database: an onshore-offshore database for regional assessment of seismic hazard and tectonic evolution.

Geochemistry, Geophysics, Geosystems 23, e2022GC010425. https://doi.org/10.1029/2022gc010425 v.
Wölbern, I., Rümpker, G., Schumann, A., Muwanga, A., 2010. Crustal thinning beneath the Rwenzori region, Albertine rift, Uganda, from receiver-function analysis. International Journal of Earth Sciences 99, 1545–1557. https://doi.org/10.1007/s00531-009-0509-2 v.
Wolfenden, E., Ebinger, C., Yirgu, G., Renne, P.R., Kelley, S.P., 2005. Evolution of a Volcanic Rifted margin: Southern Red Sea, 117. Geological Society of America Bulletin, Ethiopia, p. 846. https://doi.org/10.1130/B25516.1 v.
Zuza, A.V., Yin, A., Lin, J., Sun, M., 2017. Spacing and strength of active continental strike-slip faults. Earth. Planet. Sci. Lett. 457, 49–62. https://doi.org/10.1016/j.epsl.2016.09.041 v.